

SMALL SCALE PERMEABILITY MEASUREMENTS AT ELEVATED PRESSURES: ANALYSIS AND CORRECTION OF EXPERIMENTAL ERROR USING MICRO XRAY-CT

S.M. Alizadeh¹, N. Francois², J. Middleton², S. Latham², A. Limaye², T. Senden², and C.H. Arns¹

¹School of Petroleum Engineering, University of New South Wales, Sydney, Australia

²Department of Applied Mathematics, Research School of Physical Sciences and Engineering, Australian National University, Canberra, Australia

This paper was prepared for presentation at the International Symposium of the Society of Core Analysts held in Napa Valley, California, USA, 16-19 September, 2013

ABSTRACT

The experimental measurement of permeability on small samples with rough surfaces under high confining pressure is subject to significant errors caused by boundary effects. These include the performance of various sleeve materials as well as core damage through coring and uneven compaction across the sample. Thus, under these conditions it is difficult to accurately measure permeability as function of applied stresses/strains. In this work we use samples of Bentheimer and Castlegate sandstone as well as Mt Gambier limestone and a sucrosic dolomite. Plugs with diameters between 5mm and 7mm are cut and placed into a purpose-built tri-axial cell on a micro-CT rotation stage. The plugs are surrounded radially by a sleeve separating confining fluid from the samples and axially by fluid distribution heads made of steel which also supply the axial load. We consider hydrostatic confinement and acquire images as well as measure permeability first at low confining pressure, then at high confining pressure, and again at low confining pressure (unloaded).

Using the high-resolution images taken at different confining pressures we calculate permeability numerically on the samples at full plug scale using a lattice Boltzmann method. We include the sleeve boundary in the calculation, which was segmented out separately to allow matching exactly the experimental boundary conditions. The resulting velocity fields are used to locally calculate the fluxes in different regions of interest. We consider partitions of the pore space based on topological distance (pores) and geometric distance with regard to the sleeve boundary. This allows calculating intrinsic permeability as function of sleeve distance to characterize the radial dependency of permeability across the core.

We observe clear fluid bypassing at the sleeve-sample interface for all samples. For the less consolidated samples (e.g. Castlegate sandstone), core damage at the outer rim is also evident, since the radial dependency shows first a maximum at the sleeve boundary, but then a minimum before stabilizing at larger sleeve distances. This is likely due to compaction either from drilling the sample or from flattening the sleeve-core interface at higher confining pressures.

The numerical approach integrated with experiment allows deriving permeability-deformation relationships without boundary effects through the development of corrections for experimental measurements. Thus, a quantitative high-resolution analysis of deformation mechanisms impacting on permeability is feasible with this combined approach by numerically eliminating experimental errors.

INTRODUCTION

The measurement of permeability on small rock samples compared to an intrinsic length scale of the samples is an important problem and poses several challenges, in particular if also considering the influence of stress boundary conditions on permeability. Common practice is to use cylindrical samples and apply either a pressure drop across the sample or inject with a constant flow rate. Provided the flow is in the laminar regime, Darcy's law is then employed to calculate the absolute permeability of the rock by considering measurements at several flow rates. To ensure that no flow bypasses the rock sample, a sleeve is usually used to seal the sample and prevent communication between permeating and confining fluid. There are few works, which consider the effect of sleeve type with confining pressure and rock texture on permeability measurements. Stewart and Unalmsir [1] found that there could be a considerable error in measuring the porosity of sandstones due to the imperfect sealing at the boundary of rock and sleeve. Profice et al. [2] pointed out the difficulty of measuring the permeability of tight sandstones or shale gas reservoir rocks due to the narrow and poorly percolating pore network of such rocks. Lenormand et al. [3] measured the permeability of small rock samples utilizing a variety of methods and mentioned problems arising from the leakage of gas from the space between rock and the surrounding silicon tube used to make the measurements. They suggested adding a heat shrinkable layer to tighten up the annulus space minimizing the error associated with leakage. McPhee and Arthur [4] considered conventionally-derived Klinkenberg parameters and factors that affect the permeability measurements like sleeve material, net effective stress, transducer error etc. over a wide range of permeabilities. According to them, the sleeve pressure for the "ambient" condition measurement of the permeability of rocks is not a standardized value, but can vary from 150 psi up to 800 psi. For low permeability of the rock and/or high fluid viscosity high pore pressures may develop in the rock, resulting in a reduced effective confining pressure and possibly poorer conformance of the sleeve with the rock sample. The lack of universal agreement on a standard confining pressure combined with the different sleeve materials used for permeability measurements complicates comparisons between measurements made in different laboratories.

In recent years there is increasing interest in the pore scale features of reservoir rocks, as many transport properties are controlled by features on the micron scale. Over the last decade, micro Xray-CT methods have been established as a viable choice for the numerical derivation of permeability [5-7]. However, small cores are typically required and this should increase the effects of the choice of sleeve materials, if the size of the boundary region of the sample in terms of a characteristic length scale of the sample is significant. This is an important consideration if a direct comparison of numerical

simulation and experiment is desired. This direct comparison is more important if heterogeneous rock samples are considered, since one can otherwise for each technique choose a sample size (and resolution), which is still at a representative elementary volume (REV), but minimizes experimental (large sample) or numerical (high resolution) error. Furthermore, if a direct comparison is possible, numerical techniques can be used to avoid some of the systematic experimental problems while also enabling the study of the effects of deformations mechanisms on permeability at the pore scale.

In this work we consider the effect of sleeve conformance on permeability measurements for four rock samples, Bentheimer and Castlegate sandstone, Mt Gambier limestone, and a sucrosic dolomite, under hydrostatic stress conditions. Physical measurements of permeability are coupled with Lattice-Boltzmann computations of permeability for pre- and post-stress conditions. To assess the contribution of different regions within the sample to the total flux, we introduce sample partitions based on distance to the sleeve boundary using either direct geometric distance or a pore-based topological criterion.

METHODS

In the following we describe the techniques required for analyzing the local contribution of fluxes to the total flux through the sample. We first characterize the samples, followed by a short description of the experimental setup, and the permeability calculation and analysis of the resulting velocity fields using topological and geometric partitions.

Sample Characterization

In this study we consider a sample each of Bentheimer and Castlegate sandstone, Mt Gambier limestone, and a sucrosic dolomite. Bentheimer sandstone is a clean clastic rock, the mineral phase of our plug (plug porosity 24%, diameter 6mm) consisting of 98.5% quartz and 1.5% kaolinite according to XRD analysis. XRD measurements on Castlegate (plug porosity 19%, diameter 7mm) returned 74% quartz, 17% feldspar, 7% kaolinite, and 2% calcite and magnesium. Mt. Gambier limestone is a monomineralic heterogeneous rock (plug porosity 54%, diameter 6 mm). Finally, the sucrosic dolomite is a relatively homogeneous carbonate sample with feature sizes of the order of the two sandstones, exhibiting grains with high angularity (plug porosity 17.5%, diameter 5 mm). The length to diameter ratio of all samples was about 2. Cross-sections of the tomograms of the samples are depicted in Figure 1.

Experimental Procedure

We utilize the high-resolution ANU/UNSW micro Xray-CT facility in Canberra [8]. The system has recently been equipped with a specialized high-pressure tri-axial cell made of Beryllium. A purpose build rotary joint enables connecting flow lines and application of axial load, while at the same time permitting indefinite rotation (see Figure 2). The samples were wrapped into a heat-shrinkable transparent fluoropolymer sleeve with maximum operating temperature of 150°C and shrink ratio of 2:1. The tensile strength was given by the manufacturer as 24.1MPa with secant Young modulus of 172MPa. The thickness of the sleeve prior to heat-shrink is approximately 0.3mm. Each sample is

placed into the pressure cell and loaded hydrostatically to initial stress conditions of 200 psi effective confining pressure. After a stress equilibration time of 1h a high-level vacuum is applied, followed by brine saturation and permeability measurement using a 0.5M brine solution (0.3M sodium chloride, 0.2M sodium iodide). A high-resolution tomogram is then acquired in this stress state. The resulting raw tomograms, which include the sleeve boundaries, were then subjected to standard image processing steps using the in-house software “mango”, described in more detail in [9]. The top row of Figure 3 depicts cross-sections of the segmented samples including the sleeve boundaries at low confining pressure.

Permeability Calculation

The calculation of permeability from micro Xray-CT images can conveniently be carried out by making use of the natural discretisation of the sample into cubic voxels. We apply the D3Q19 model of the lattice Boltzmann approach [10-12,5,6] with periodic boundary conditions in the flow direction, adding a 30 voxel thick free fluid layer to make the core plugs periodic. Side boundary conditions are given naturally by the imaged sleeve. Full plug simulations were carried out using our MPI-parallel implementation (“morphy”) with Cartesian decomposition on 512 to 1024 cores and check-pointing set to 3h intervals. Cuts through sections of some of the resulting velocity fields are given in Figure 4 using “Drishti” for the visualization of the vector fields [13,14].

Local Flux Analysis

The LBK algorithm is deriving the solution of the Navier-Stokes equation for an incompressible fluid. Thus, one can derive the local contribution to the flux of the fluid through any voxel by a local analysis of the velocity field or the contribution of a region by considering a voxel subset. We use two different order fields to carry out such an analysis. Our interest is in quantifying the influence of the sleeve boundary on the flux. The distance to the sleeve boundary is expressed topologically by calculating the distance from the sleeve boundary as the number of pores to cross. The alternative geometric method is to simply use the Euclidean distance to the sleeve boundary. Defining equidistant intervals on the Euclidean distance map by introducing a shell thickness ΔR , we derive an order variable from the Euclidean distance map allowing for significant statistics (see Figure 5).

Rather than calculating the permeability and average velocity for the full field of view, we can now calculate the contribution of each region to the total flux by defining the permeability k_i of a region i given by Darcy’s law:

$$\langle v \rangle_i = \frac{-k_i \langle \nabla p \rangle}{\mu}$$

where μ is the dynamic viscosity, v the velocity in a voxel, p the pressure, and $\langle \rangle$ indicates a volume average, e.g. [12]. Here we consider the average of the z-component of the velocity only, which is in the direction of the applied body force.

RESULTS

We present in Figure 6 the regional flux contribution to the absolute permeability of the considered samples using the Euclidean distance to the sleeve boundary as partitioning field for open (sleeve) and closed (epoxy-filled) boundary side conditions. For all four samples there is a large spike in flux close to the sleeve boundary for open boundary conditions, which is reduced to 0 when the boundary is epoxy filled. Comparing also to Figure 7 the boundary region extends over about (70 voxel distance to sleeve or 0.44mm, boundary region 24% of sample volume) for Bentheimer sandstone, (100 voxel, 0.64mm, 33% of sample) for Castlegate sandstone, (100-180 voxel, 0.34mm-0.61mm, 21%-37% of sample) for Mt Gambier limestone, and (160 voxel, 0.86mm, 57% of sample) for the sucrosic dolomite. Nevertheless, the quasi-radial profile of permeability across the sample shows that the permeability recovers to a stable value for all samples when using Euclidean distance to describe the radial profile. For Bentheimer this plateau is relatively flat, while for Mt Gambier and the sucrosic dolomite significant fluctuations remain, indicating larger heterogeneity. The radial profile using topological distance shows an eventual trend towards zero at large topological distance for the heterogeneous samples. This can be explained by the presence of pore-throat correlations and the crossing of a series of small pores, as a series of large pores maps to small topological distances.

We further calculate the permeability ratio calculated with open and closed boundary conditions for the four samples; Bentheimer: $3.0D/2.0D = 1.5$, Castlegate: $4.29D/0.28D = 15$ (!), Mt. Gambier: $7.9D/3.7D = 2.1$, and sucrosic dolomite: $0.91D/0.69D = 1.3$.

For Castlegate sandstone there appears to be an extended damaged zone at initial stress conditions illustrated by the downward drop of permeability along the quasi-radial profile before an almost linear upwards trend reaches a plateau relatively deep into the sample. This damage could be the result of the plug coring procedure, as Castlegate is poorly consolidated and the coring process might rip out grains, while pushing others into the rock. Figure 8 depicts Castlegate sandstone pre- and post-loading conditions (after loading hydrostatically to 1700 psi). The eminent trend has been removed by the loading cycle. This indicates a reorientation/homogenization of the sample through the applied stress conditions, which will be the focus of a forthcoming paper.

CONCLUSIONS

The extent of boundary effects for absolute permeability measurements on the considered small samples is large and needs to be taken into account, e.g. in upscaling procedures by selecting sub-volumes away from boundaries during high-resolution rock-typing or by including the sleeve effect to compare with experiments. A separation of boundary effects and rock-specific representative fluid flow is possible using micro-CT imaging. Well-defined numerical permeabilities can be derived at sample scale by filling the sleeve cavity numerically. This is important for high-pressure work, as the sample does not need to be filled with epoxy from the sides, which might change the outcome of an analysis of deformation effects on permeability in tri-axial test.

ACKNOWLEDGMENTS

The authors acknowledge the member companies of the Digital Core Consortium and the National Computing Infrastructure (NCI) for their support. CHA acknowledges the Australian Research Council for a Future Fellowship.

REFERENCES

1. Stewart, R.W. and Unalmsir, S., “Boundary effect on porosity measurement and its resolution by method and mathematical means”, *The Log Analyst*, (1989), **30**, 85–92.
2. Profice, S., Lasseux, D., Jannot, M.Y., Jebara, N., Hamon, G., “Permeability, porosity and Klinkenberg coefficient determination on crushed porous media”, *Society Of Core Analysts*, Austin, Texas, 18 - 21 September 2011.
3. Lenormand, R., Bauget, F., Ringot, G., “Permeability measurements on small rock samples”, *Society of Core Analysts*, Halifax, Nova Scotia, Canada, 4-7 October 2010.
4. McPhee, C.A., Arthur, K.G., “Klinkenberg permeability measurements: problems and practical solutions”, *Advances in Core Evaluation: Accuracy and Precision in Reserves Estimation*, Ed. PF Worthington, (1991), 447–462.
5. Spanne, P., Thovert, J., Jacquin, J., Lindquist, W. B., Jones, K., Adler, P. M., “Synchrotron computed microtomography of porous media: topology and transports”, *Phys. Rev. Lett.*, (1994), **73**, 2001-2004.
6. Arns, C.H., Knackstedt, M.A., Pinczewski, W.V., Martys, N.S., “Virtual permeametry on microtomographic images”, *Journal of Petroleum Science and Engineering*, (2004), **45**, 12, 41 – 46.
7. Ramstad, T., Oren, P.E., Bakke, S., “Simulation of two phase flow in reservoir rocks using a lattice Boltzmann method”, *Proceedings of the SPE Annual Technical Conference and Exhibition*, (2009), **4**, 2561–2576.
8. Sakellariou, A., Arns, C.H., Sheppard, A.P., Sok, R.M., Averdunk, H., Limaye, A., Jones, A.C., Senden, T.J., Knackstedt, M.A., “Developing a virtual materials laboratory”, *Materials Today*, (2007), **10**, 12, 44–51.
9. Sheppard, A.P., Sok, R.M., Averdunk, H., “Techniques for image enhancement and segmentation of tomographic images of porous materials”, *Physica A: Statistical Mechanics and its Applications*, (2004), **339**, 12, 145–151.
10. Bhatnagar, P.L., Gross, E.P., Krook, M., “A model for collision processes in gases. I. small amplitude processes in charged and neutral one-component systems”, *Physical Review*, (1954), **94**, 511–525.
11. Qian, Y. H., d'Humieres, D., Lameland, P., “Lattice BGK models for Navier-Stokes equation”, *Europhys. Lett.*, (1986), **2**, 291.
12. Martys, N. S., Chen, H., “Simulation of multicomponent fluids in complex three-dimensional geometries by the lattice Boltzmann method”, *Phys. Rev. E*, **53**, 743-750.
13. Cabral, B., Leedom, L.C., “Imaging vector fields using line integral convolution”, In:

Proceedings of the 20th annual conference on Computer graphics and interactive techniques. SIGGRAPH '93, New York, ACM, 1993:263–270.

14. Limaye, A.. “Drishti: a volume exploration and presentation tool”, *Proc. SPIE 8506, Developments in X-Ray Tomography VIII*, (2012), doi:10.1117/12.935640.

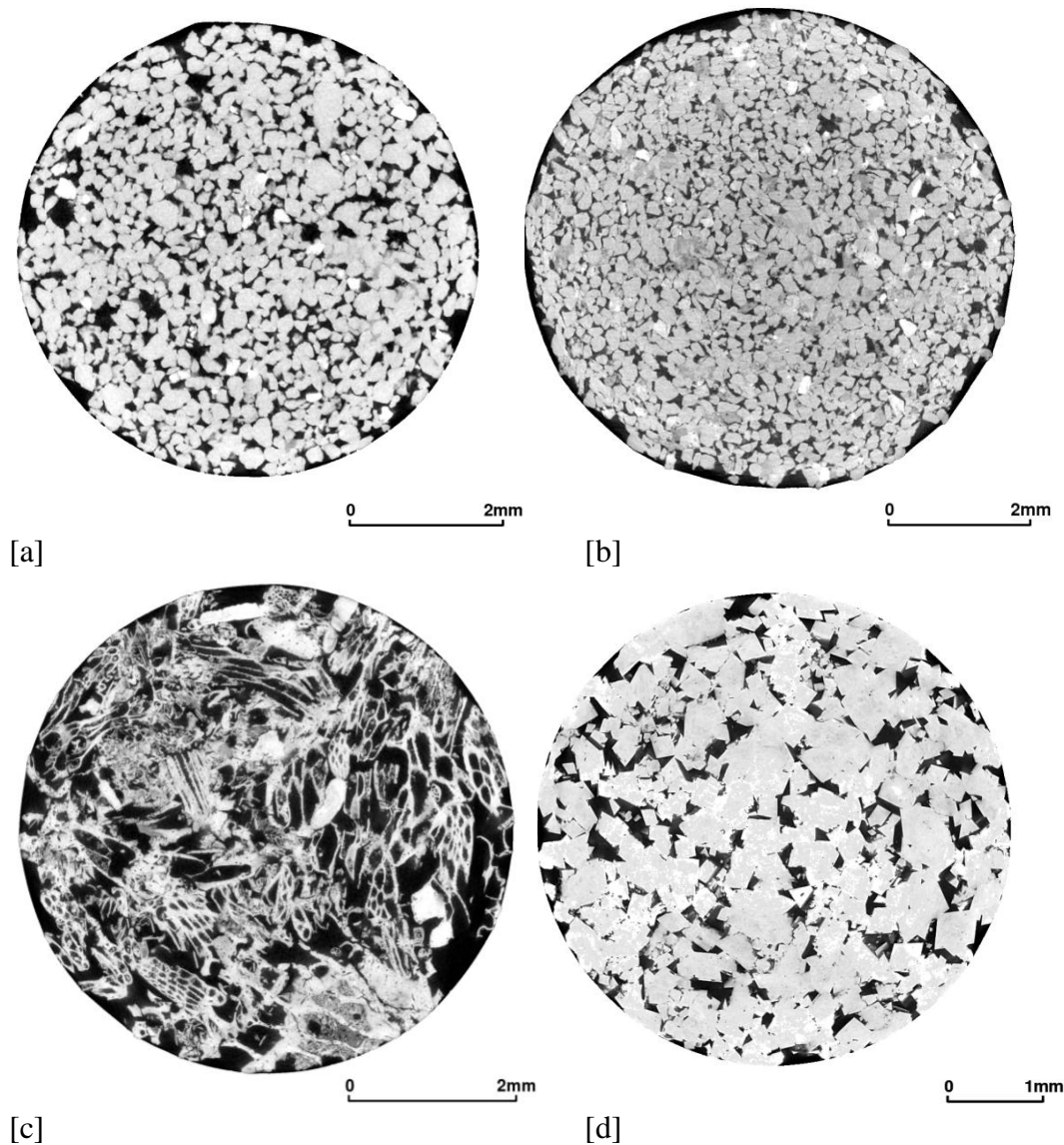


Figure 1: Cross-sections of the raw tomograms of the samples used in this study (\emptyset : plug diameter, ε : resolution). [a] Bentheimer sandstone ($\emptyset=7\text{mm}$, $\varepsilon=6.28\mu\text{m}$), [b] Castlegate sandstone ($\emptyset=7\text{mm}$, $\varepsilon=6.43\mu\text{m}$), [c] Mt Gambier limestone ($\emptyset=6\text{mm}$, $\varepsilon=3.39\mu\text{m}$), [d] sucrosic dolomite ($\emptyset=5\text{mm}$, $\varepsilon=5.4\mu\text{m}$). All tomograms are acquired with field of view of 2048^3 voxels including sleeve boundary and pressure cell.



Figure 2: Micro Xray-CT imaging setup with mounted tri-axial cell. 1: End shaft and rotary joint, 2: Beryllium cell, 3: confining pressure port, 4: rotation stage, 5: CCD camera, 6: shutter, 7: Xray source.

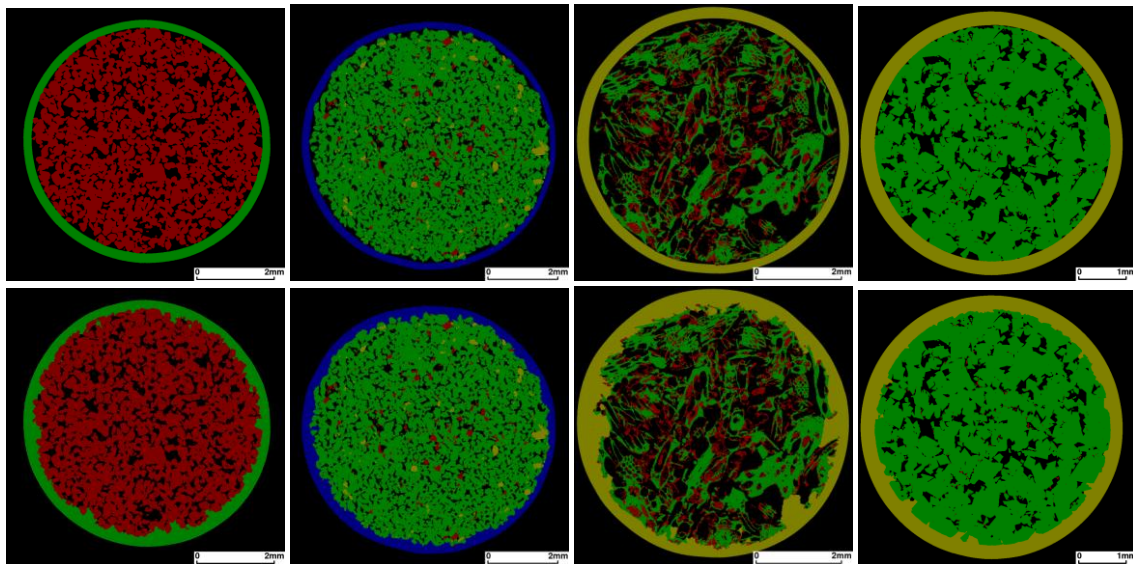


Figure 3: Cross-sections through the segmented images of this study under ambient conditions (pre-deformation). *From left to right:* Bentheimer sandstone, Castlegate sandstone, Mt Gambier limestone, sucrosic dolomite. *Top:* segmentation with original sleeve boundary. *Bottom:* The open pore space on the boundary has been filled using a topological criterion by filling all pores touching the sleeve.

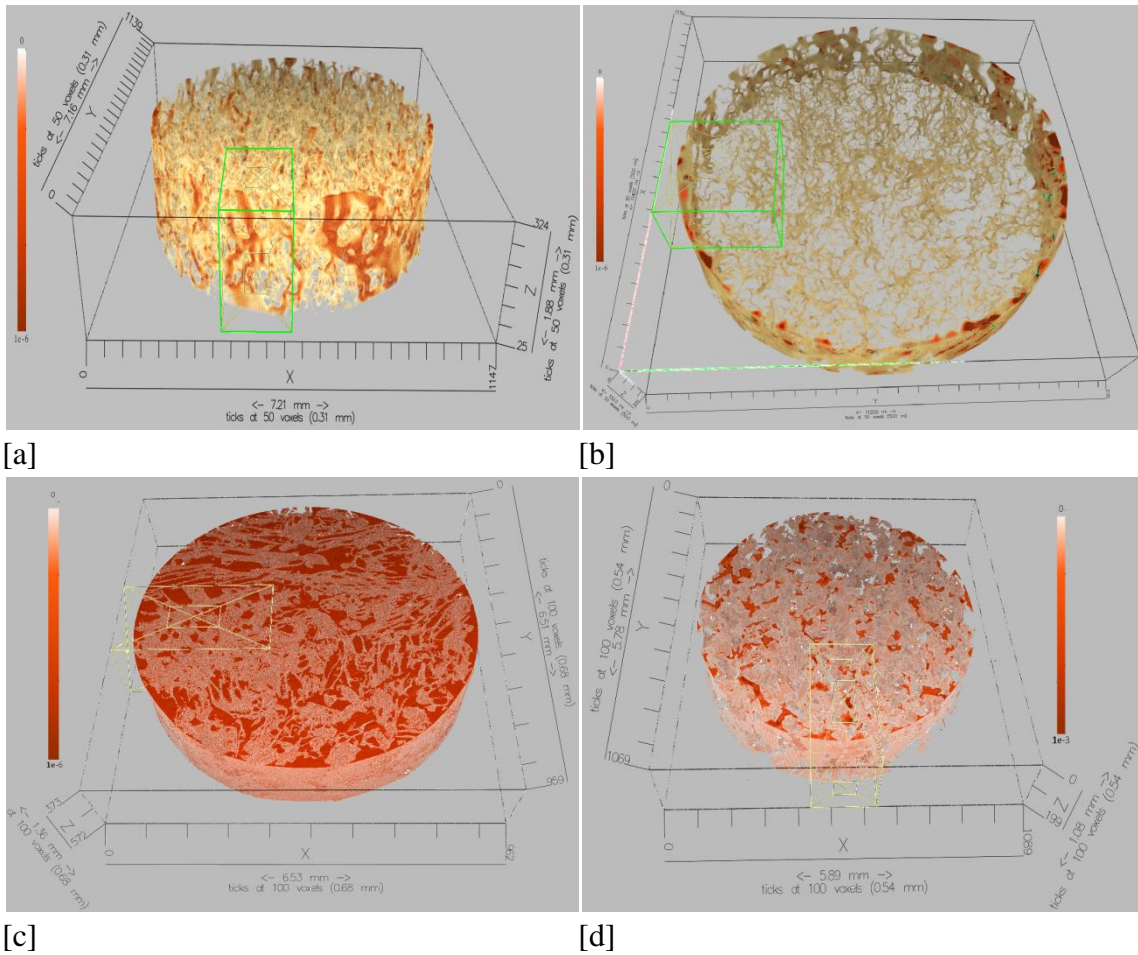


Figure 4: Visualisation of subsections of the velocity fields: [a] Bentheimer sandstone, [b] Castlegate sandstone, [c] Mt. Gambier limestone, and [d] sucrosic Dolomite.

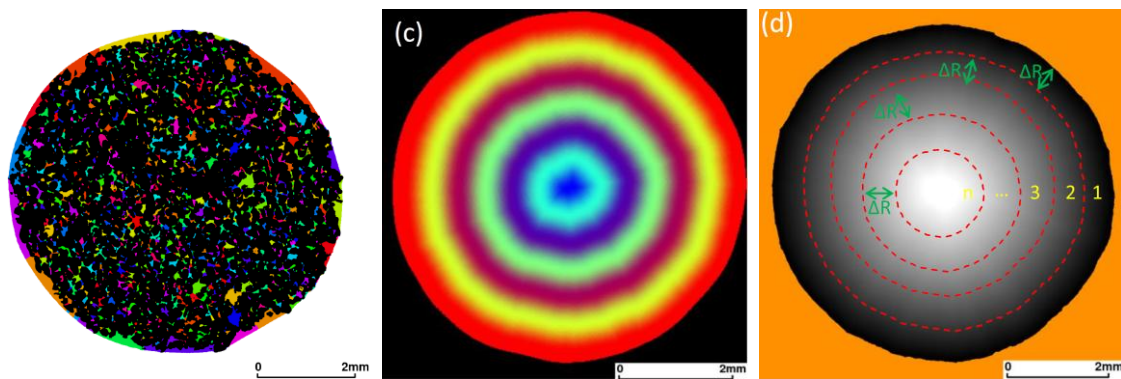


Figure 5: Illustration of topological and geometric partitions with relation to the sleeve boundary for Bentheimer sandstone (colours are used to highlight different pores). *Left*: pore partitioning, *middle*: Euclidean distance, *right*: thresholding of the Euclidean distance maps to define shells of thickness ΔR .

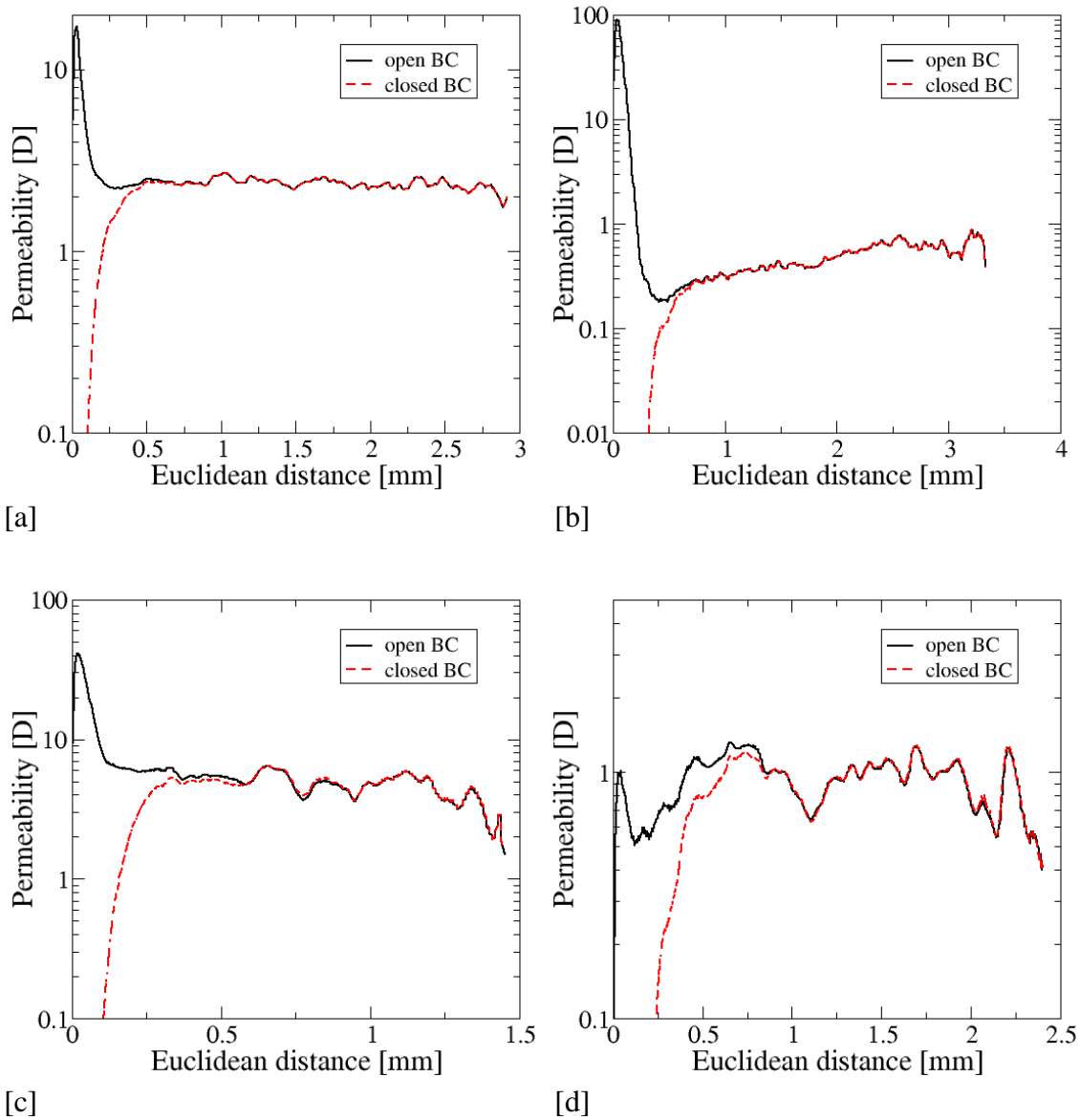


Figure 6: Regional analysis of the flux fields using geometrical shells based on the Euclidean distance map. [a] Bentheimer sandstone, [b] Castlegate sandstone, [c] Mt. Gambier limestone, [d] sucrosic dolomite. Each plot shows the results of two simulations for the full imaged core, comparing flux fields under experimental boundary conditions using the imaged sleeve (“open boundary”) with the closed boundary conditions (“epoxy”) realized by topologically closing the outermost pores (see Figure 3). Large sub-volumes of the samples (20%-50%) are affected by boundary effects, but unaffected regions are clearly observed.

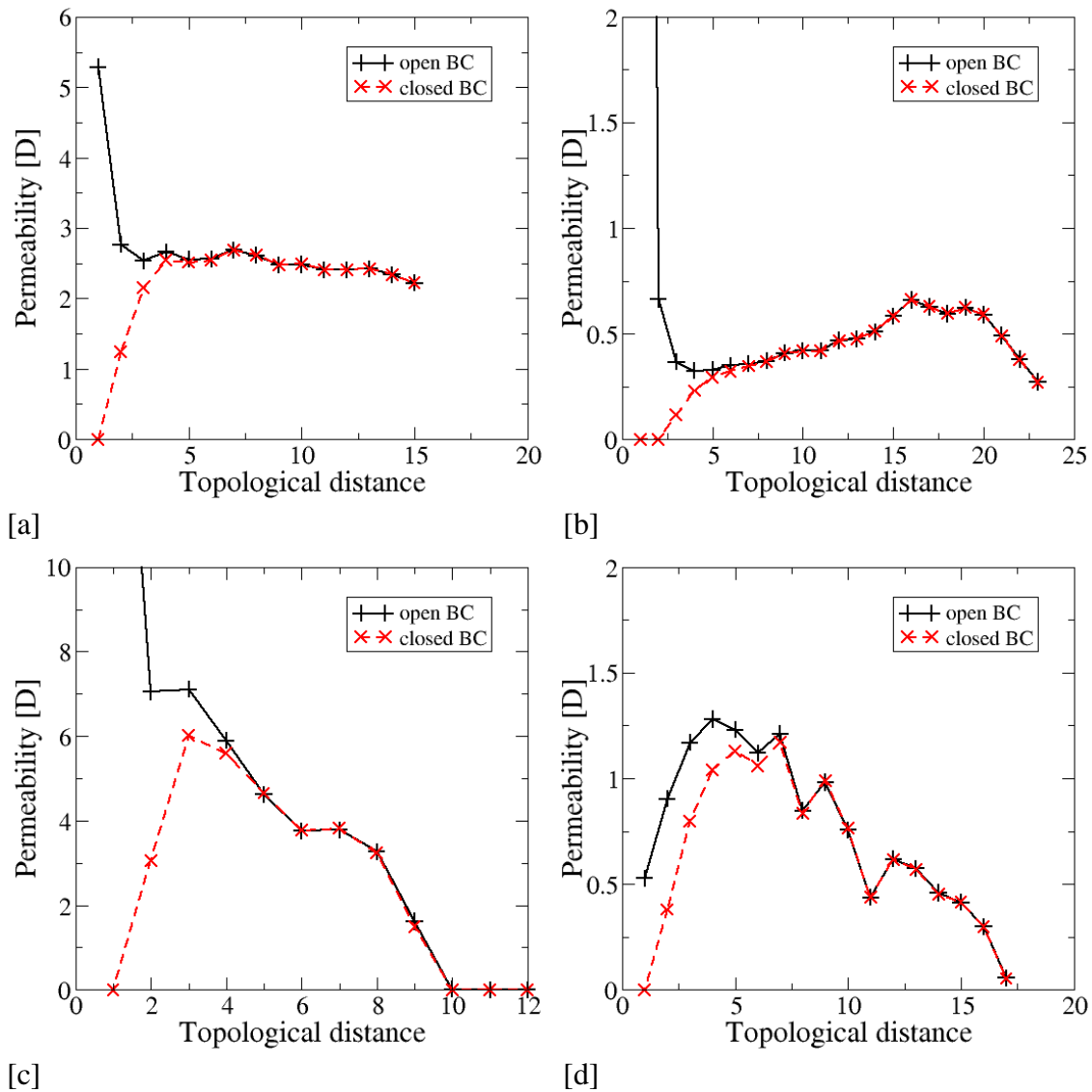


Figure 7: Regional analysis of the flux fields using topological shells based on the pore partitioning. The topological distance is defined with regard to the number of pores crossed counting from the sleeve boundary. Pores of topological distance one directly contact the sleeve. [a] Bentheimer sandstone, [b] Castlegate sandstone, [c] Mt Gambier limestone, [d] sucrosic dolomite. Each plot shows the results of two simulations for the full imaged core, comparing flux fields under experimental boundary conditions using the imaged sleeve (“open boundary”) with the closed boundary conditions (“epoxy”) realized by topologically closing the outermost pores (see Figure 3).

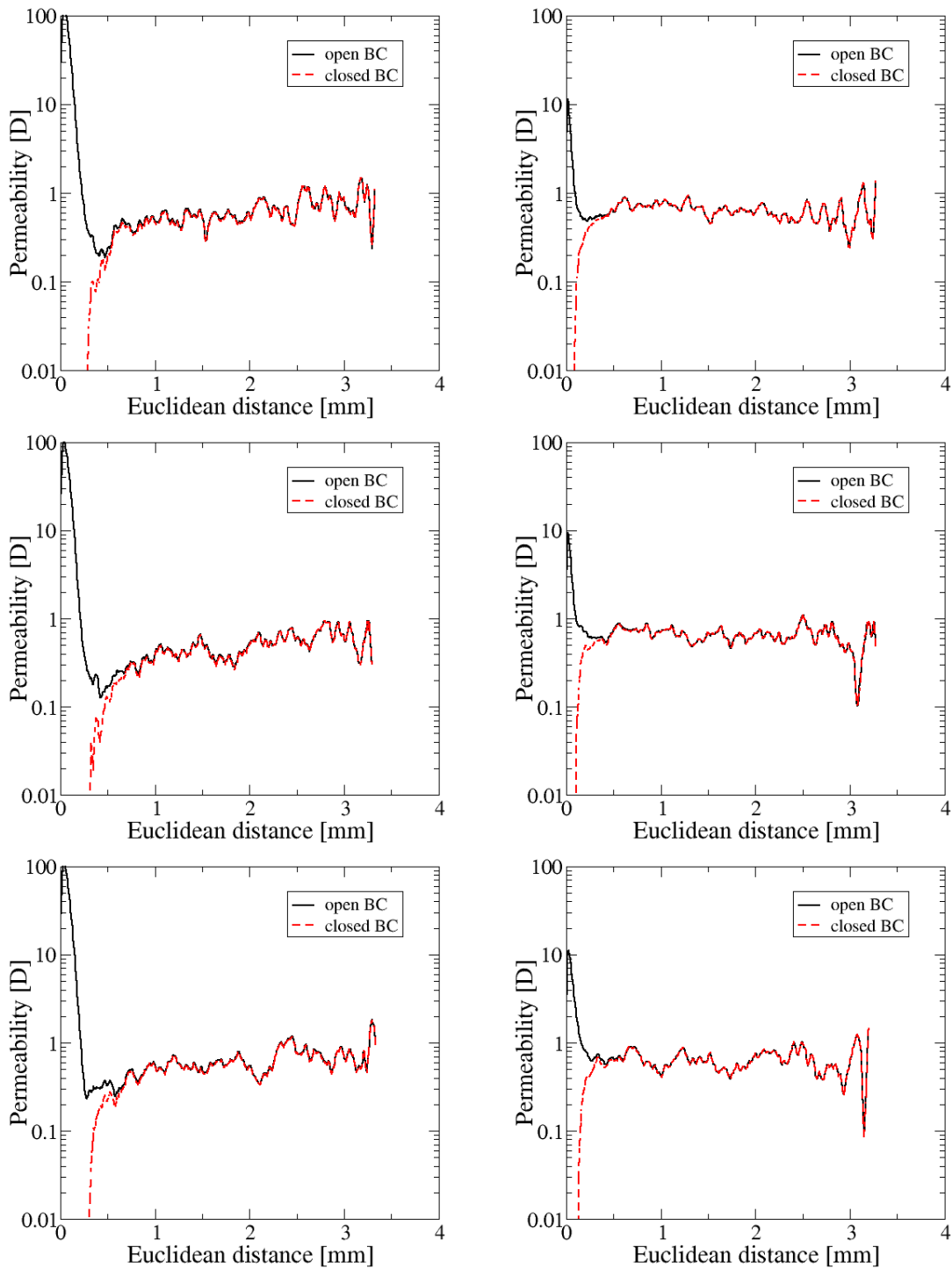


Figure 8: Regional analysis of the flux fields for Castlegate Sandstone using geometric shells based on the Euclidean distance map. *Left*: Pre-loading conditions, *Right*: post-loading conditions. From top to bottom: slabs 1, 3, and 5: cylindrical cross-sections of 300 voxel thickness.